

Assimilation of T-TREC-Retrieved Winds from Single-Doppler Radar with an Ensemble Kalman Filter for the Forecast of Typhoon Jangmi (2008)

Mingjun Wang^{1,2}, Ming Xue^{1,2,3}, Kun Zhao¹ and Jili Dong²

¹Key Laboratory for Mesoscale Severe Weather/MOE and School of Atmospheric Science, Nanjing University, Nanjing, China 210093

²Center for Analysis and Prediction of Storms, and ³School of Meteorology, University of Oklahoma, Norman, Oklahoma, 73072

December, 2013

Submitted to Monthly Weather Review

* *Corresponding author address:*

Dr. Ming Xue

Center for Analysis and Prediction of Storms

University of Oklahoma

120 David Boren Blvd, Norman OK 73072

E-mail: mxue@ou.edu

Abstract

A tropical cyclone (TC) circulation Tracking Radar Echo by Correlation technique (T-TREC) developed recently is applied to derive horizontal winds from single Doppler radar reflectivity Z data (combined with radial velocity V_r data when available). The typically much longer maximum range of Z observations compared to V_r data allows for much larger spatial coverage of the T-TREC retrieved winds (V_{TREC}) when a TC first enters the maximum range of a coastal radar. Retrieved using data from more than one scan volume, the T-TREC winds also contain valuable cross-beam wind information. The V_{TREC} or V_r data at 30 min intervals are assimilated into the ARPS model at 3 km grid spacing using an ensemble Kalman filter, over a 2-hour window shortly after Typhoon Jangmi (2008) entered the V_r coverage area of an operational weather radar of Taiwan. The assimilation of V_{TREC} data produces analyses of the typhoon structure and intensity that more closely match observations than analyses produced using V_r data or the reference GFS analysis. Subsequent 28-hour forecasts of intensity, track, structure, and precipitation are also improved by assimilating V_{TREC} data. Further sensitivity experiments show that assimilation of V_{TREC} data can build up a reasonably strong vortex in 1 hour, while a longer assimilation period is required to spin up the vortex when assimilating V_r . Although the difference between assimilating V_{TREC} and V_r is smaller when the assimilation window is longer, the improvement from assimilating V_{TREC} is still evident. Assimilating Z data in addition to V_r or V_{TREC} results in little further improvement.

1 **1. Introduction**

2 Doppler weather radar is an important instrument for observing landfalling
3 tropical cyclones (TCs) at high spatial and temporal resolutions. In recent years, radial
4 velocity (V_r) and/or radar reflectivity (Z) data from ground-based coastal Doppler radars
5 have been assimilated into high-resolution numerical weather prediction (NWP) models
6 to improve TC forecasts, primarily using a three-dimensional variational (3DVAR) data
7 assimilation (DA) system (e.g., Xiao et al. 2007; Zhao and Jin 2008; Zhao and Xue 2009;
8 Zhao et al. 2012a; Zhao et al. 2012b) or an ensemble Kalman filter (EnKF) (e.g., Zhang
9 et al. 2009; Dong and Xue 2013 (DX13 hereafter); Xue and Dong 2013). Compared with
10 3DVAR using static background error covariance, the EnKF can estimate flow-dependent
11 background error covariance through an ensemble of forecasts and theoretically has
12 significant advantages for TC analysis (Zhang et al. 2009; Hamill et al. 2011).

13 For typical S-band operational weather surveillance radars, including the WSR-
14 88D of the United States and the CINRAD-98D of China, the maximum range of V_r
15 measurements is 230 km, limiting radar coverage of TCs when they are located far from
16 the coast. The maximum range of Z measurements of these radar systems extends about
17 twice as far, providing potentially very useful information before the core region of the
18 TC moves into the V_r coverage area. The assimilation of Z has produced positive impacts
19 on hurricane analysis and forecasting within 3DVAR frameworks (Xiao et al. 2007; Zhao
20 and Jin 2008; Zhao and Xue 2009), but V_r data generally have larger impacts than Z data
21 for TC initialization (Zhao and Jin 2008; Zhao and Xue 2009; DX13).

22 Apart from providing direct information on precipitation, reflectivity has been
23 used to derive wind fields within TCs using the tracking radar echoes by correlation

24 (TREC) method, assuming that reflectivity changes between two successive radar volume
25 scans are mainly caused by advection (Tuttle and Gall 1999). Harasti et al. (2004)
26 modified the TREC technique for the real-time wind analysis of TCs at different altitudes.
27 Recently, Wang et al. (2011) developed the TC circulation TREC (T-TREC) technique
28 by extending TREC to polar coordinates (centered on the TC) and constraining the local
29 echo tracking region using the vortex rotation rate estimated from available V_r data. T-
30 TREC has been used for diagnosing TC circulations in realtime at the China
31 Meteorological Administration (CMA).

32 V_r only contains the along-beam component of the wind field, thus when
33 assimilating V_r from a single radar the cross-beam components of winds are often
34 retrieved poorly (Zhao et al. 2012a; Zhao et al. 2012b). The full three-dimensional wind
35 field retrieved from a single Doppler radar can, however, be valuable for TC initialization.
36 Zhao et al. (2012a) investigated the impact of assimilating GBVTD (Ground Based
37 Velocity Track Display) retrieved winds from a single Doppler radar, and found that
38 doing so resulted in an improved analysis and forecast of a typhoon compared to an
39 analysis obtained by assimilating V_r data directly. The cross-beam wind component and
40 more-complete spatial coverage provided by GBVTD-retrieved winds in the TC inner
41 core region were the primary reasons for the better performance of GBVTD-retrieved
42 winds compared to V_r . The drawback with GBVTD retrievals is that the data do not
43 contain asymmetric wind components beyond wavenumber 3, therefore more detailed
44 asymmetric structures present in V_r data may be lost. Retrieved from two time levels of
45 three-dimensional Z observations, the T-TREC winds (V_{TREC}) are not subject to such
46 limitations; they contain retrieved cross-beam winds and generally have a much wider

47 data coverage area than V_r (because of the typically longer range of Z compared to V_r for
48 operational radars) and GBVTD-retrieved winds (which are derived from V_r
49 observations). For these reasons, V_{TREC} data have the potential to improve the analysis
50 and initialization of the inner core structures of TCs approaching landfall.

51 Recently, Li et al. (2013) explored the assimilation of V_{TREC} winds using the
52 WRF 3DVAR system (Barker et al. 2004; Xiao et al. 2005) for the analysis and forecast
53 of Typhoon Meranti (2010) before it made landfall at Fujian Province at the southeast
54 coast of China. They assimilated V_{TREC} or V_r data from a single coastal radar at a single
55 time approximately 8, 6, 4, or 2 hours prior to landfall. Their results indicate that
56 assimilation of V_{TREC} data leads to better analysis of the structure and intensity of the
57 typhoon than directly can be obtained assimilating V_r data. The subsequent forecasts for
58 the typhoon track, intensity, structure, and precipitation are also improved, although the
59 differences become smaller for the latter analysis times when V_r data coverage improves
60 as the typhoon approaches the radar. The larger spatial coverage of V_{TREC} data and the
61 cross-beam information it contains are believed to be the primary reasons for the superior
62 performance of V_{TREC} over V_r data.

63 Parallel to the effort of Li et al. (2013), this study examines the impact of cycled
64 assimilation of V_{TREC} data on the analysis and forecasting of Typhoon Jangmi (2008),
65 using an ensemble Kalman filter (EnKF) at a convection-permitting resolution. Typhoon
66 Jangmi made landfall on the east coast of Taiwan on 28 September 2008. Before and
67 during its landfall, the TC inner core was observed by an operational S-band Doppler
68 radar located at Hualian, Taiwan, from 0000 UTC 28 September to 0000 UTC 29
69 September. In this study, the retrieved V_{TREC} data are assimilated using EnKF through

70 30-minute assimilation cycles for 1 to 3 hours prior to Jangmi entered the observation
71 range of Hualian radar. The impacts of assimilating V_{TREC} data on the track, intensity,
72 structure, and precipitation forecasts are examined, and the analyses thus obtained are
73 compared with analyses obtained by assimilating V_r data directly. The impact of
74 assimilating reflectivity data in addition to V_{TREC} or V_r data is also examined.

75 The rest of this paper is organized as follows. Section 2 describes the forecast
76 model, radar data, and experimental design. The results of the first set of experiments that
77 assimilate radar data for 2 hours are first presented in section 3, together with discussions
78 on the impacts of the radar data on the analyses and forecasts. Section 4 presents the
79 results of sensitivity experiments that examine the impacts of assimilation window length
80 (of 1 or 3 hours) and reflectivity assimilation. Conclusions and discussions are presented
81 in Section 5.

82

83 **2. Model, radar data, and experimental design**

84 *a) The prediction model*

85 The Advanced Regional Prediction System (ARPS; Xue et al. 2000; Xue et al.
86 2001) version 5.3 is used as the prediction model. The physical domain is $2400 \times 2400 \times 25$
87 km^3 and has a 3 km horizontal grid spacing (Fig. 1). A stretched vertical grid is used; the
88 mean vertical grid spacing is 500 m, with a minimum vertical spacing of 20 m near the
89 surface. Full model physics are used, including the Lin ice microphysics scheme (Lin et
90 al. 1983), Goddard Space Flight Center (GSFC) long- and short-wave radiation
91 parameterization, a two-layer force-restore soil-vegetation model (Ren and Xue 2004),
92 1.5-order turbulent kinetic energy (TKE)-based subgrid-scale turbulence (Deardorff 1980)

93 and PBL parameterization (Xue et al. 1996). For this study in particular, a new surface
94 flux parameterization scheme for the ocean surface based on Makin (2005) is
95 implemented into the ARPS and used in this study. Different from the original scheme in
96 the ARPS, based on (Anderson 1993) and having the drag coefficient linearly increasing
97 with the surface wind speed (see, Xue et al. 1995), the new scheme reduces the drag
98 coefficient for wind speeds exceeding 33 m s^{-1} based on field measurement data (Powell
99 et al. 2003). This new scheme is found to allow for the prediction of larger surface wind
100 speeds than the original formulation, though the overall intensity of the analyzed and
101 predicted typhoon is not substantially changed in our experiments. The initial analysis
102 background and the lateral boundary conditions (LBCs) are obtained from the National
103 Centers for Environmental Prediction (NCEP) operational Global Forecast System (GFS).

104

105 *b) Radar data processing and quality control*

106 The V_r and Z data from Hualian radar on the east coast of the Taiwan Island
107 (HLRD, Fig. 1) are first manually edited, including velocity dealiasing and ground clutter
108 removal. To retrieve V_{TREC} , Z and V_r data are first interpolated to a grid with 1 km grid
109 spacing in both horizontal and vertical; the retrieval is performed within a 300 km radius
110 of the TC center at each level from 1 to 8 km. To keep the retrieved V_{TREC} data mostly
111 independent, the retrieval was performed on a grid with horizontal grid spacing of 10 km,
112 and the retrieved data are directly assimilated. More details on the T-TREC technique can
113 be found in Wang et al. (2011). When assimilating V_r data for comparison, the data are
114 interpolated in the horizontal to the ARPS model columns but kept on radar elevation
115 levels in the vertical.

116 The V_{TREC} data at 3 km above the surface at 0000 UTC, 28 September 2008, are
117 shown along with the observed Z in Fig. 3a, along with observed V_r in Fig. 3b, and along
118 with the V_r simulated from V_{TREC} data (by projecting to the radar radial directions) in Fig.
119 3c. Observed V_r is limited to a maximum range of 230 km, resulting in an incomplete
120 velocity dipole pattern with areas of missing data (Fig. 3b). T-TREC retrieves the cross-
121 beam velocity and fills the V_r data voids quite effectively (Fig. 3a). The simulated V_r
122 shows a similar pattern as the observed V_r within the 230 km radius, suggesting that
123 V_{TREC} (including the cross-beam component) estimates are reasonably accurate both
124 within and outside of the V_r coverage area (Fig. 3c). The root-mean-square error of
125 simulated V_r against the observed V_r is about 3.8 m s^{-1} during the 3-hour DA window
126 (see Fig. 2), which is consistent with the corresponding error statistics of less than 4 m s^{-1}
127 from data samples examined in Wang et al. (2011). During EnKF DA, observation error
128 standard deviations for V_r and V_{TREC} are specified as 2 m s^{-1} and 5 m s^{-1} , respectively,
129 guided by the error statistics of our data samples.

130

131 *c) EnKF experiments and settings*

132 A baseline control forecast (CNTL) without radar DA is run from 0000 UTC 28
133 to 0600 UTC 29 September, initialized from the National Centers for Environmental
134 Prediction (NCEP) operational Global Forecast System (GFS) analysis (Table 1).
135 Following DX13, an initial forecast ensemble is generated by adding mesoscale
136 perturbations at 1800 UTC 27 September and convective perturbations at 2330 UTC, 30
137 min before the first radar DA (see Fig. 2), giving a 6-hour ensemble spin-up period prior

138 to DA. For additional details about the mesoscale and convective perturbations used, we
139 refer the reader to DX13.

140 All DA experiments start from 0000 UTC 28 September and use 30-min
141 assimilation cycles. For the first set of two DA experiments, ExpTREC2H and ExpVr2H,
142 V_{TREC} and V_r data are assimilated within a 2-hour window (Table 1, Fig. 2). This specific
143 DA period is chosen because it is a period during which the main circulation of Jangmi
144 was fully covered by Z data but not by V_r data (Fig. 3). The assimilation period is
145 relatively short in order to maximize the forecast lead time prior to landfall of the
146 typhoon; studies have also shown that it is usually the first few assimilation cycles for
147 radar data that have the largest impact on TC initialization (DX13; Li et al. 2012). To
148 further examine the impact of the DA window on the analysis and forecast, two
149 additional pairs of experiments, ExpVr1H (ExpVr3H) and ExpTREC1H (ExpTREC3H)
150 are run. These experiments are the same as ExpVr2H and ExpTREC2H except that they
151 perform data assimilation for a period of 1 hour (3 hours) starting at the same time (Table
152 1, Fig. 2). In another pair of experiments, ExpVrZ2H and ExpTRECZ2H, radar
153 reflectivity observations are assimilated in addition to V_r or V_{TREC} within a 2-hour
154 window. At the end of the assimilation window of each experiment, a deterministic
155 forecast is launched and run until 0600 UTC 29 September. The workflows of the DA
156 experiments are illustrated in Fig. 2.

157 Considering the different observation densities (Zhang et al. 2009; Torn 2010),
158 covariance localization radii of 50 (10) km in the horizontal and 4 km in the vertical are
159 used when assimilating V_{TREC} (V_r) data. A posterior relaxation-to-prior adaptive
160 covariance inflation (Whitaker and Hamill 2012) with $\alpha=0.9$ is applied at those model

161 grid points directly influenced by observations to help maintain the ensemble spread. In
162 addition to experience obtained from DX13, sensitivity experiments were performed to
163 arrive at the current optimized DA configuration.

164 The deterministic forecasts are verified against the best track data and
165 precipitation observations. During the verification period, which extends from 0000 UTC
166 28 September to 0600 UTC 29 September, best track data from the Japan Meteorological
167 Agency (JMA), Taiwan Central Weather Bureau (CWB), and Joint Typhoon Warning
168 Center (JTWC), have significant differences; standard deviations of track, minimum sea
169 level pressure (MSLP), and maximum surface wind (MSW) are as large as 31 km, 10 hPa,
170 and 8 m s^{-1} , respectively. Uncertainties in best track estimates are also well recognized in
171 recent studies (Torn and Snyder 2012; Landsea and Franklin 2013). In this study, average
172 best track (ABT) data from these three operational centers is used for verification.

173

174 **3. EnKF analyses and deterministic forecasts**

175 *a) EnKF analyses of typhoon circulations and structures*

176 The horizontal winds at 3 km above the surface after the first EnKF analysis at
177 0000 UTC are shown in Fig. 4b-c for ExpVr2H and ExpTREC2H, together with the
178 horizontal winds in the initial condition of CNTL, which are interpolated from GFS
179 analysis valid at the same time (Fig. 4a). The vortex in the GFS analysis is too broad,
180 with a radius of maximum wind (RMW) in excess of 100 km (Fig. 4a). In ExpVr2H, the
181 RMW is only about 30 km, with the strongest winds found northeast and southwest of the
182 eye (Fig. 4b). These strong winds are mostly in the radial direction of the HLRD radar,
183 suggesting that the cross-beam wind component is under-estimated in ExpVr2H. The
184 inability of EnKF to accurately analyze the cross-beam wind component from single-

185 Doppler radial velocity data was also noted in DX13; suspected causes include relatively
186 poor quality of the background error covariance derived from ensemble forecasts of
187 typhoons that are too weak, and possible prediction model error. More investigation of
188 this problem is warranted in future studies, but such investigation is beyond the scope of
189 the current study.

190 In ExpTREC2H, the vortex is much stronger than in ExpVr2H with a more
191 continuous azimuthal circulation. The wind field does exhibit a prominent wavenumber-1
192 asymmetry structure, with the maximum of 45 m s^{-1} located in the northeastern quadrant
193 (Fig. 4c), co-located with a region of strong convection observed by HLRD (Fig. 3a).

194 Fig. 4d-f show the sea-level pressure (SLP) and surface wind speed of the CNTL
195 forecast and the final EnKF analyses of ExpVr2H and ExpTREC2H at 0200 UTC. The
196 simulated vortex in CNTL has a MSLP of 986 hPa, much higher than the ABT value of
197 920 hPa (Fig. 4d). The MSLP of ExpVr2H is at 973 hPa while ExpTREC2H has the
198 lowest value at 936 hPa, only 16 hPa above the ABT estimate. The circulation around the
199 eyewall in ExpTREC2H is stronger than in both CNTL and ExpVr2H, with an annulus of
200 wind speeds exceeding 30 m s^{-1} around the center. ExpTREC2H also has the smallest
201 position error (approximately 5 km).

202 To examine the vertical structure of the analyzed vortices, the azimuthally-
203 averaged tangential wind and temperature anomaly are presented in Fig. 4g-i. The
204 temperature anomaly is defined as the deviation from the horizontal average within a 180
205 km radius (Liu et al. 1999). The vortex circulations of CNTL (Fig. 4g) and ExpVr2H
206 (Fig. 4h) are weak and broad. ExpTREC2H (Fig. 4i) has a much tighter, stronger, and
207 deeper vortex, with a RMW of only 30 km and a 30 m s^{-1} wind speed contour that

208 extends as high as 8 km above the surface. The maximum temperature anomaly in
209 ExpTREC2H is approximately 14 K at 6 km above the surface in the eye of the typhoon,
210 suggesting a much stronger warm core than in either CNTL or ExpVr2H. Although the
211 vertical structure cannot be directly verified by observation, the warm core structure is
212 consistent with recent observation and simulation studies (Halverson et al. 2006; Stern
213 and Nolan 2011) in terms of general warm core structure. The V_{TREC} data build a stronger
214 vortex than V_r data, due to the much more complete vortex circulation within the V_{TREC}
215 data.

216

217 *b) Impacts on track and intensity predictions*

218 The predicted typhoon tracks, track errors, MSLPs, and MSWs from CNTL,
219 ExpVr2H, and ExpTREC2H are plotted along with the ABT in Fig. 5. From 0200 UTC
220 28 September to 0600 UTC 29 September, Jangmi moved first to the northwest, then
221 turned westward toward Taiwan. The track turned northwestward soon after landfall, then
222 turned north-northeastward after the center passed over Taiwan (Fig. 5a). All three turns
223 occur in the forecast of ExpTREC2H at locations close to those indicated in the ABT
224 data, except for the final turn, which is substantially delayed. The track forecast of
225 ExpTREC2H has a mean error of 51 km (Fig. 5b). The track of CNTL has the most
226 westward bias, with a mean track error of approximately 65 km. ExpVr2H has the most
227 northward track bias early on and lacks the initial westward and northwestward turns,
228 resulting in a mean track error of about 66 km (Fig. 5b). Overall, ExpTREC2H has the
229 smallest track error.

230 The MSLPs and MSWs from all three experiments are plotted along with those of
231 the ABT in Fig. 5c and Fig. 5d, respectively. Starting from a relatively weak vortex with
232 a MSLP of 986 hPa, the typhoon intensity in CNTL does not change much during the
233 forecast period, resulting in a mean MSLP error of 28 hPa and an error as large as 65 hPa
234 at the initial condition time (0200 UTC). The intensity forecast is somewhat improved in
235 ExpVr2H, but the mean MSLP error is still as large as 22 hPa during the forecast period
236 and the initial error is around 53 hPa. In comparison, ExpTREC2H has a much smaller
237 mean MSLP forecast error of about 11 hPa, and an initial error of only about 16 hPa;
238 starting from a much lower initial MSLP, ExpTREC2H captures well the weakening of
239 the typhoon as it makes landfall around 0800 UTC (Fig. 5c). Consistent with the much
240 improved MSLP, the analyzed and predicted MSW in ExpTREC2H also show clear
241 improvement compared to the other experiments (Fig. 5d). The initial MSW at 0200 UTC
242 in ExpTREC2H is about 43 m s^{-1} , about 10 m s^{-1} higher than in ExpVr2H and CNTL; this
243 difference is maintained for about 12 hours. ExpTREC2H captures the weakening phase
244 of the typhoon quite well. These results again show clear benefit of assimilating V_{TREC}
245 data, even though there is still some intensity error (weak bias) in the final analysis of this
246 very intense typhoon.

247

248 *c) Impacts on the forecast of typhoon structure*

249 To examine the impact of V_{TREC} and V_r assimilation on Jangmi's structure in the
250 forecast, the predicted composite reflectivity (column maximum) and horizontal wind
251 vectors at 3 km height are presented in Fig. 6 for all three experiments, together with the
252 observed composite reflectivity. At 0500 UTC, Jangmi has a rather compact eye with

253 heavy precipitation in the southern and eastern quadrants of the vortex. The simulated
254 typhoon in CNTL has a broad, elliptical eyewall with overly-intense reflectivity (Fig. 6d).
255 The eye in ExpVr2H is tighter and more circular, but still too large (Fig. 6g). The forecast
256 typhoon in ExpTREC2H, which features the strongest predicted intensity, has a tighter
257 vortex with a smaller eye (Fig. 6j) than that of ExpVr2H, and even contains some inner-
258 core rainbands that appear to match radar observations (Fig. 6a). Similar to observations,
259 precipitation in ExpTREC2H is most widespread in the southern and eastern quadrants of
260 the storm.

261 In the 9-hour forecast (after Jangmi has made landfall), the eye of the typhoon has
262 filled in with precipitation, and the strongest echo (>35 dBz) regions are located primarily
263 over Taiwan (Fig. 6b). The inner-core precipitation over land is disrupted in CNTL, with
264 an overly-broad outer spiral rainband over the ocean (Fig. 6e). ExpVr2H (Fig. 6h) has a
265 tight vortex over land and disorganized precipitation bands, while ExpTREC2H features
266 the tightest vortex and inner rainbands located over Taiwan (Fig. 6k), including a north-
267 south heavy precipitation band (due to interaction with the Central Mountain Range or
268 CMR) located further east than in the observations (Fig. 6b). At 1700 UTC, the observed
269 precipitation is highly asymmetric, and the strongest echoes are mostly located over
270 southern Taiwan along the CMR (Fig. 6c). In all experiments, reflectivity patterns over
271 land (Fig. 6f, i, l) agree well with the observations due to interactions with the mountain
272 range. In general, the rainbands in ExpTREC2H are closer to the typhoon center,
273 resulting in better agreement with the observations than in CNTL and ExpVr2H, whose
274 precipitation distributions are too broad. In summary, the assimilation of V_{TREC} or V_r data
275 improves the predicted structure of Jangmi, and the best agreement with observations in

276 terms of the predicted rainband structures and precipitation distributions occurs in
277 ExpTREC2H.

278

279 *d) Precipitation forecasts*

280 The 12-hour accumulated precipitation and the corresponding equitable threat scores
281 (ETS) valid at 1400 UTC 28 September from all experiments are plotted in Fig. 7
282 together with the precipitation observations. The observed rainfall is obtained from
283 quantitative precipitation estimation and segregation using multiple sensor (QPESUMS,
284 Gourley et al. 2002) system data provided by the Central Weather Bureau of Taiwan.
285 Prominent in the data is a strong precipitation band along the CMR (Fig. 7a). Two
286 precipitation maxima are located over north and central Taiwan. These maxima are
287 significantly under-predicted in ExpVr2H and CNTL (Fig. 7b, c), but better captured in
288 ExpTREC2H, with the greatest improvement occurring for the northern maximum (Fig.
289 7d). ExpTREC2H also produces the highest ETSS (0.47, 0.41, and 0.35) for thresholds of
290 40 mm, 80 mm, and 120 mm, respectively. In summary, ExpTREC2H produces the best
291 precipitation forecast both in terms of distribution and magnitude; these relatively good
292 predictions can be attributed to the accuracy of track, intensity, and structure forecasts of
293 the typhoon.

294

295 **4. Sensitivity experiments**

296 The experiments presented earlier used a 2-hour long assimilation window with
297 30 min DA cycles. To determine whether the conclusions regarding the relative impacts
298 of T-TREC versus Vr data still hold when data are assimilated at different window

299 lengths, two additional pairs of experiments are performed using 1 h and 3 h assimilation
300 windows. Another question one may ask is: when radar reflectivity data are also
301 assimilated, does the relative impact of V_{TREC} and V_r data change? This question is
302 examined through two experiments that are identical with ExpVr2H and ExpTREC2H
303 except for the addition of Z data (Table 1).

304

305 *a) Sensitivity to assimilation window length*

306 Experiments ExpVr1H (ExpVr3H) and ExpTREC1H (ExpTREC3H) are the same
307 as ExpVr2H and ExpTREC2H, respectively, except that the length of time during which
308 DA is performed is changed to 1 hour (3 hours). We can also consider ExpVr1H
309 (ExpTREC1H) and ExpVr2H (ExpTREC2H) part of the longer DA experiment ExpVr3H
310 (ExpTREC3H) with the difference being the time at which the forecast is launched. A
311 summary and comparison of experiments is presented in Table 1.

312 Analyses and forecasts of MSLP and MSW during the assimilation cycles from
313 0000 to 0300 UTC are plotted in Fig. 8 to examine the direct impacts of data assimilation
314 on typhoon intensity. ABT data and the CNTL forecast are also plotted for comparison.
315 At the end of the 1-hour assimilation window, the MSLP readings in ExpVr1H and
316 ExpTREC1H decrease by 3 hPa and 45 hPa, respectively; these values are 6 hPa and 48
317 hPa lower than that of CNTL experiment, respectively. Over the next 2 hours, when
318 assimilating V_{TREC} , MSLP remains between 936 and 937 hPa, resulting in errors of 16
319 hPa to 17 hPa against the ABT data. When assimilating V_r , the MSLP decreases from
320 980 hPa to 962 hPa, resulting in an error of around 42 hPa compared to ABT data at the
321 end of the DA period.

322 The MSW of ExpTREC2H (Fig. 8b) increases by about 11 m s^{-1} during the first
323 EnKF analysis (time = 0 in the figure), while the MSW increment in ExpVr2H is very
324 small. Assimilation of V_r only has a small impact on the MSW until later cycles, due to
325 the limited number of near-surface inner-core observations of V_r early in the experiment.
326 The MSW in the V_{TREC} assimilation experiments increases to about 48 m s^{-1} after one
327 hour of assimilation (60 min in the figure), 18 m s^{-1} higher than the MSW in the V_r
328 assimilation experiments at the corresponding time. MSW later remains relatively steady
329 in the V_{TREC} experiments, decreasing slightly to 43 m s^{-1} at 120 min, then increasing
330 slightly to 45 m s^{-1} at 180 min. Throughout the 3 hours, the MSW in the V_{TREC}
331 experiments consistently remains approximately 10 m s^{-1} higher than the MSW in the V_r
332 assimilation and CNTL experiments; the stronger analyzed surface vortex in the V_{TREC}
333 experiments more closely matches the best track intensity.

334 Generally, as the number of assimilation cycles (and thus the length of
335 assimilation window) increases, the differences in analyses produced using V_{TREC} and V_r
336 assimilation becomes smaller, but even after 3 hours of assimilation the analyzed vortex
337 in ExpTREC3H remains much stronger than that of ExpVr3H, with MSLP and MSW
338 differences between the experiments of 25 hPa and 10 m s^{-1} , respectively. Overall,
339 assimilating V_{TREC} can effectively build up a strong typhoon vortex using a shorter data
340 assimilation period; for realtime forecasting this would permit a longer forecast lead time
341 prior to typhoon landfall. It takes much longer for V_r to establish the typhoon vortex, and
342 the resultant vortex is weaker even after three hours of DA.

343 We note from Fig. 8 that assimilation of V_{TREC} data is very effective in increasing
344 the MSW, especially in the first analysis when the background vortex is too weak (Fig.

345 8b). In comparison, the reduction to the MSLP in the first as well as other cycles is
346 minimal (Fig. 8a). To investigate how assimilation of V_{TREC} data impacts the wind and
347 pressure fields, east-west vertical cross-sections of tangential wind and pressure analysis
348 increments are plotted in Fig. 9 through the vortex center for the first analysis. Directly
349 updated by the V_{TREC} data, the vortex circulation is greatly enhanced, with a maximum
350 wind speed increment of over 45 m s^{-1} . EnKF analysis of V_{TREC} data reduces the pressure
351 near the vortex center via cross-variable correlation between wind and pressure, but the
352 maximum pressure reduction is only around 2 hPa. This rather small reduction is at least
353 partly due to the relatively small ensemble spread in the near-surface pressure field.
354 Compared to uncertainty in the wind forecast, which is relatively localized, the ensemble
355 spread of pressure in the inner core of the TC is more related to the overall TC intensity
356 uncertainty. All vortices in the background ensemble forecasts at 0600 UTC are too weak
357 compared to observations, contributing to the under-estimation of surface pressure
358 ensemble spread.

359 The lowest altitude at which V_{TREC} data is available is 1 km; below this level, the
360 tangential wind increment is achieved through spatial covariance subject to vertical
361 covariance localization. Given that the vertical localization radius used is 4 km,
362 localization reduction is relatively small at the surface. Still, spatial correlation tends to
363 decrease with distance from the observations; as a result, the wind increment at the 1 km
364 level is as large as 40 m s^{-1} , while the maximum wind increment at the surface is only
365 around 25 m s^{-1} . The MSW after the first analysis is 11 m s^{-1} (Fig. 8b); this is because
366 assimilation of V_{TREC} data also corrects the position of the strongest surface winds,

367 reducing the radius of maximum wind in the vortex from about 100 km to about 40 km
368 (not shown).

369 Most of the increase in MSW during DA is achieved in the analysis steps, while
370 most of the MSLP reduction is achieved during the forecast steps (Fig. 8). Similar
371 behavior was observed in Li et al. (2012), which used the WRF 3DVAR and WRF
372 ETKF-En3DVar hybrid system to assimilate coastal radar radial velocity data for a
373 landfalling hurricane. Almost all MSLP reductions in their experiments were also
374 achieved during the forecast steps (see their Fig. 8b). The overall MSW increases and
375 MSLP reductions are much more substantial when assimilating V_{TREC} data. V_{TREC} -
376 assimilating experiments create strong, closed circulations much more quickly than
377 experiments assimilating V_r data (Fig. 8c, Fig. 4c). However, because the analysis step
378 creates large wind increments but very small pressure increments, the balance of the
379 analyzed wind and pressure fields may not be particularly good.

380 Within a typhoon vortex and above the boundary layer, the gradient wind balance
381 is a reasonable approximation between the wind and pressure field. To examine if and
382 how the wind and pressure fields adjust to each other during the assimilation cycles, the
383 gradient wind relation is diagnosed by calculating the residual of gradient wind balance
384 (GWR), defined as:

$$385 \quad GWR = \frac{V_T^2}{r} + fV_T - \frac{1}{\rho} \frac{\partial p}{\partial r},$$

386 where V_T is the tangential wind, p is the pressure, ρ is the air density, f is the Coriolis
387 parameter, and r is the radius from vortex center. The root-mean-squared (RMS) GWRs
388 are calculated and plotted every kilometer from 0 – 12 km above the surface within a 300
389 km radius of the typhoon for analyses and forecasts during the DA period in Fig. 10. The

390 calculation region is chosen to cover the main circulation of the typhoon; most of the
391 direct impact of radar DA is confined to this region.

392 A higher value of RMS GWR means more wind-pressure imbalance, and vice
393 versa. In general, the assimilation of V_{TREC} or V_r data induces imbalance between wind
394 and pressure, but this imbalance is quickly reduced during the subsequent model forecast.
395 The RMS GWR is increased from 0.001 to more than 0.02 m s^{-2} during the first analysis
396 of V_{TREC} data (Fig. 10); this result is consistent with the significant increase in MSW with
397 only a small reduction in MSLP noted in Fig. 8. After 30 min of forecast time, the RMS
398 GWR is reduced to about 0.003 m s^{-2} , and after 1 h, the RMS GWRs in analyses and
399 forecasts stabilize, remaining below 0.01 and 0.005 m s^{-2} , respectively, suggesting that
400 the model pressure field in these later cycles has adjusted to match the vortex present in
401 the wind field. As a result, no large discrepancy arises during the later cycles when the
402 wind field is directly updated by the V_{TREC} assimilation, again demonstrating the ability
403 of V_{TREC} assimilation to quickly build up a strong, balanced vortex through frequent DA
404 cycles. In comparison, assimilation of V_r data creates less imbalance, due to much
405 smaller wind increments. The RMS GWR increases slightly during assimilation in the V_r
406 experiment, which may be due to the increased V_r data coverage, but remains below 0.01
407 and 0.005 m s^{-2} for the analyses and forecasts, respectively. This investigation indicates
408 that even through the analyzed pressure and wind fields are not well-balanced, especially
409 when the wind increments are large, the pressure field can rather quickly adjust to the
410 strengthened wind fields during the subsequent forecast step, especially when a strong
411 vortex circulation is established in the analysis steps.

412 The predicted track, track error, MSLP, and MSW for ExpVr1H, ExpVr2H,
413 ExpVr3H, ExpTREC1H, ExpTREC2H and ExpTREC3H are plotted in Fig. 11. For
414 experiments assimilating V_r for varying lengths of time, the track forecasts show similar
415 paths (Fig. 11a). The mean track errors are 67, 66, and 65 km in ExpVr1H, ExpVr2H,
416 and ExpVr3H, respectively (Fig. 11b). The predicted tracks from ExpTREC1H,
417 ExpTREC2H, and ExpTREC3H are similar, but their mean track errors of 50, 51, and 57
418 km are smaller than those of the V_r -assimilating experiments (Fig. 11a, b). When
419 assimilating V_r , due to the improved intensity analyses obtained when using a longer DA
420 period, intensity forecasts are also improved, with mean MSLP errors of 26, 22 and 20
421 hPa in ExpVr1H, ExpVr2H and ExpVr3H, respectively (Fig. 11c). In comparison, the
422 MSLP forecasts from ExpTREC1H, ExpTREC2H, and ExpTREC3H are not sensitive to
423 the assimilation window length; all have a much lower mean error of around 11 hPa.
424 Consistent with the improved MSW analysis, the MSW forecasts from the V_{TREC}
425 assimilation experiments agree better with observations than those of the experiments
426 assimilating V_r data (Fig. 11d). The mean MSW errors from ExpTREC1H, ExpTREC2H,
427 and ExpTREC3H are 6.9, 5.6 and 5.0 $m\ s^{-1}$ lower than those of ExpVr1H, ExpVr2H, and
428 ExpVr3H, respectively. These results again show the advantage of assimilating V_{TREC}
429 data as opposed to V_r data, particularly for shorter assimilation window lengths.

430

431 *b) Sensitivity to assimilation of reflectivity*

432 In ExpVrZ2H and ExpTRECZ2H, reflectivity data are assimilated alongside V_r
433 or V_{TREC} from 0000 to 0200 UTC using EnKF (see Table 1) to investigate whether the
434 relative impact of V_r and V_{TREC} is changed when Z data are included. Similar to DX13,

435 our sensitivity experiments showed that using reflectivity to update the wind, potential
436 temperature, and water vapor mixing ratio had a negative impact on the analysis (not
437 shown). Therefore, reflectivity data are used to update only pressure and microphysical
438 variables in our experiments. Compared to the assimilation of V_r or V_{TREC} in ExpVr2H
439 and ExpTREC2H, the assimilation of additional Z data has little impact on the intensity
440 analyses and forecasts (Fig. 12). The track forecasts of ExpVrZ2H and ExpTRECZ2H
441 (Fig. 12a) are similar to those ExpVr2H and ExpTREC2H. The mean track errors are 63
442 and 52 km for ExpVrZ2H and ExpTRECZ2H, comparable to those of ExpVr2H and
443 ExpTREC2H. The ETSs of 12-hour accumulated precipitation are 0.34 and 0.49 for
444 ExpVrZ2H and ExpTRECZ2H at the 40 mm threshold, and 0.13 and 0.32 at the 120 mm
445 threshold, respectively; these values are similar to those obtained in ExpVr2H and
446 ExpTREC2H (Fig. 7). Overall, assimilation of Z data does not substantively alter the
447 relative impacts of V_r and V_{TREC} assimilation.

448

449 **5. Conclusions and discussions**

450 Radar reflectivity (Z) data have been used to retrieve winds using the recently
451 developed TC circulation Tracking Radar Echo by Correlation (T-TREC) technique,
452 which, in our implementation, also uses V_r observations to limit the correlation search
453 region when available. This study examines, for the first time, the impact of cycled
454 assimilation of T-TREC retrieval winds (V_{TREC}) on TC analysis and forecasting using an
455 EnKF. Typhoon Jangmi, which passed over Taiwan during September of 2008, is chosen
456 as a test case. Radar data from a single coastal operational weather radar at Hualian,
457 Taiwan, are assimilated prior to typhoon landfall.

458 V_{TREC} or V_r data are assimilated at 30 min intervals during a 2-hour window
459 shortly after the typhoon entered the V_r coverage region of the Hualian operational radar.
460 The assimilation of V_{TREC} data improves the intensity and structure of the typhoon
461 significantly, while the assimilation of V_r data over the same time period yields a much
462 smaller improvement due to limited V_r data coverage and poor retrieval of the cross-
463 beam wind component. The improved analyses obtained by assimilating V_{TREC} data
464 allows for better track, intensity, structure, and precipitation forecasts. Secondly, four
465 sensitivity experiments using data assimilation periods of different lengths are performed.
466 Results show that V_{TREC} assimilation can quickly (within 1 hour) build up a strong vortex,
467 while a longer period of cycled data assimilation is required when using V_r data to spin
468 up the vortex. While the difference between V_{TREC} and V_r assimilation is smaller as the
469 length of data assimilation increases, even after 3 hours of data assimilation the analysis
470 and forecasts obtained by assimilating V_{TREC} data are still much better than those
471 obtained by assimilating V_r .

472 Assimilation of V_{TREC} (and, to a lesser extent, V_r) data effectively updates the
473 wind fields and creates large wind increments in early data assimilation cycles, though
474 the associated pressure increments are much smaller, resulting in an imbalance between
475 the analyzed wind and pressure. Gradient wind balance diagnoses are performed to show
476 that the pressure field can adjust quickly and efficiently to the enhanced wind fields,
477 especially in the V_{TREC} assimilation experiments. As a result, MSLP reduction can be
478 achieved during the forecast steps of the EnKF, since strong vortex circulations have
479 already been established by the radar data assimilation.

480 Finally, when Z data are assimilated alongside V_r or V_{TREC} for two hours in
481 another pair of experiments, the relative impact of V_r and V_{TREC} assimilation is
482 unchanged. Overall, due to more complete wind information (including the retrieved
483 cross-beam component) and a larger spatial coverage of data, V_{TREC} assimilation is more
484 effective than V_r assimilation, and can potentially provide good TC initialization and
485 improved forecasts several hours earlier than V_r observations can as a TC approaches the
486 coast. Although the conclusions here are based on a single landfalling typhoon case, the
487 results obtained by assimilating V_{TREC} and V_r data for different lengths of time appears to
488 be robust. More cases should be examined to confirm these conclusions in the future.

489 Compared to the single-time assimilation of V_{TREC} data for Typhoon Meranti
490 (2010) in Li et al. (2013) using WRF 3DVAR, this study examines the impact of cycled
491 assimilation of V_{TREC} data using an EnKF on the analysis and forecast of the intense
492 typhoon Jangmi (2008). Consistent with Li et al. (2013), our results demonstrate the
493 ability of V_{TREC} assimilation to quickly build up a strong vortex. In this study, the
494 assimilation of V_{TREC} at the first analysis time also significantly improves the vortex
495 circulation in the analysis, while subsequent cycles further improve the typhoon analysis
496 and facilitate the establishment of a balanced vortex through wind-pressure adjustment.

497 A few other issues are worthy of future exploration. T-TREC-retrieved winds
498 have a larger spatial coverage than GBVTD-retrieved winds, but may have less accuracy
499 in the inner-core region of the TC for low-wave-number components. Thus, it would be
500 interesting to compare assimilation of T-TREC and GBVTD retrieval winds. V_r data are
501 not directly used for T-TREC wind retrieval; therefore V_r is mostly independent of V_{TREC} .
502 Thus, it may be possible to assimilate both V_r and V_{TREC} together to obtain better

503 analyses than could be obtained assimilating V_{TREC} alone. It would also be interesting to
504 compare the assimilation of V_{TREC} data and the assimilation of V_r data from multiple
505 radars in a case where a typhoon is covered by multiple coastal radars. Understanding the
506 relative impacts of assimilating individual data sources or their combinations using
507 assimilation periods of varying length would also be valuable. These would be good
508 topics for future studies.

509

510 *Acknowledgements* This work was primarily supported by the Social Common Wealth
511 Research Program (GYHY201006007), National Fundamental Research 973 Program of
512 China (2013CB430100 and 2009CB421502), the National Natural Science Foundation of
513 China (grants 40975011 and 40921160381), and by the U.S. Office of Naval Research
514 grant DOD-ONR N00014-10-1-0775. Dr. Nathan Snook is thanked for careful
515 proofreading and editing the manuscript.

516

517 **References**

- 518 Anderson, R. J., 1993: A Study of Wind Stress and Heat Flux over the Open Ocean by
519 the Inertial-Dissipation Method. *J. Phys. Oceanogr.*, **23**, 2153-2161.
- 520 Barker, D. M., W. Huang, Y. R. Guo, A. J. Bourgeois, and Q. N. Xiao, 2004: A Three-
521 Dimensional Variational Data Assimilation System for MM5: Implementation
522 and Initial Results. *Mon. Wea. Rev.*, **132**, 897-914.
- 523 Deardorff, J., 1980: Stratocumulus-capped mixed layers derived from a three-
524 dimensional model. *Bound. Layer Meteor.*, **18**, 495-527.
- 525 Dong, J. and M. Xue, 2013: Assimilation of radial velocity and reflectivity data from
526 coastal WSR-88D radars using ensemble Kalman filter for the analysis and
527 forecast of landfalling hurricane Ike (2008). *Quart. J. Roy. Meteor. Soc.*, **139**,
528 467-487.
- 529 Gourley, J. J., R. A. Maddox, K. W. Howard, and D. W. Burgess, 2002: An exploratory
530 multisensor technique for quantitative estimation of stratiform rainfall. *J.*
531 *Hydrometeor.*, **3**, 166-180.
- 532 Halverson, J. B., J. Simpson, G. Heymsfield, H. Pierce, T. Hock, and L. Ritchie, 2006:
533 Warm core structure of Hurricane Erin diagnosed from high altitude dropsondes
534 during CAMEX-4. *J. Atmos. Sci.*, **63**, 309-324.
- 535 Hamill, T. M., J. S. Whitaker, M. Fiorino, and S. G. Benjamin, 2011: Global Ensemble
536 Predictions of 2009's Tropical Cyclones Initialized with an Ensemble Kalman
537 Filter. *Mon. Wea. Rev.*, **139**, 668-688.
- 538 Harasti, P. R., C. J. McAdie, P. P. Dodge, W.-C. Lee, J. Tuttle, S. T. Murillo, and F. D.
539 Marks, 2004: Real-Time Implementation of Single-Doppler Radar Analysis

540 Methods for Tropical Cyclones: Algorithm Improvements and Use with WSR-
541 88D Display Data. *Wea. Forecasting*, **19**, 219-239.

542 Landsea, C. W. and J. L. Franklin, 2013: Atlantic hurricane database uncertainty and
543 presentation of a new database format. *Mon. Wea. Rev.*, **141**, 3576-3592.

544 Li, X., J. Ming, Y. Wang, K. Zhao, and M. Xue, 2013: Assimilation of T-TREC-retrieved
545 wind data with WRF 3DVAR for the short-term forecasting of typhoon Meranti
546 (2010) near landfall. *J. Geophys. Res.*, **118**, 10,361-10,375.

547 Li, Y., X. Wang, and M. Xue, 2012: Assimilation of Radar Radial Velocity Data with the
548 WRF Hybrid Ensemble–3DVAR System for the Prediction of Hurricane Ike
549 (2008). *Mon. Wea. Rev.*, **140**, 3507-3524.

550 Lin, Y.-L., R. D. Farley, and H. D. Orville, 1983: Bulk Parameterization of the Snow
551 Field in a Cloud Model. *J. Climate Appl. Meteor.*, **22**, 1065-1092.

552 Liu, Y., D.-L. Zhang, and M. K. Yau, 1999: A Multiscale Numerical Study of Hurricane
553 Andrew (1992). Part II: Kinematics and Inner-Core Structures. *Mon. Wea. Rev.*,
554 **127**, 2597-2616.

555 Makin, V. K., 2005: A Note on the Drag of the Sea Surface at Hurricane Winds. *Bound.*
556 *Layer Meteor.*, **115**, 169-176.

557 Powell, M. D., P. J. Vickery, and T. A. Reinhold, 2003: Reduced drag coefficient for
558 high wind speeds in tropical cyclones. *Nature*, **422**, 279-283.

559 Ren, D. and M. Xue, 2004: A Revised Force–Restore Model for Land Surface Modeling.
560 *J. Appl. Meteor.*, **43**, 1768-1782.

561 Stern, D. P. and D. S. Nolan, 2011: On the height of the warm core in tropical cyclones.
562 *J. Atmos. Sci.*, **69**, 1657-1680.

563 Torn, R. D., 2010: Performance of a Mesoscale Ensemble Kalman Filter (EnKF) during
564 the NOAA High-Resolution Hurricane Test. *Mon. Wea. Rev.*, **138**, 4375-4392.

565 Torn, R. D. and C. Snyder, 2012: Uncertainty of Tropical Cyclone Best-Track
566 Information. *Wea. Forecasting*, **27**, 715-729.

567 Tuttle, J. and R. Gall, 1999: A single-radar technique for estimating the winds in tropical
568 cyclones. *Bull. Amer. Meteor. Soc.*, **80**, 653-668.

569 Wang, M. J., K. Zhao, and D. Wu, 2011: The T-TREC Technique for Retrieving the
570 Winds of Landfalling Typhoons in China. *Acta Meteor. Sinica*, **25**, 91-103.

571 Whitaker, J. S. and T. M. Hamill, 2012: Evaluating Methods to Account for System
572 Errors in Ensemble Data Assimilation. *Mon. Wea. Rev.*, **140**, 3078-3089.

573 Xiao, Q., Y.-H. Kuo, J. Sun, W.-C. Lee, D. M. Barker, and E. Lim, 2007: An Approach
574 of Radar Reflectivity Data Assimilation and Its Assessment with the Inland QPF
575 of Typhoon Rusa (2002) at Landfall. *J. Appl. Meteor. Climatol.*, **46**, 14-22.

576 Xiao, Q., Ying-Hwa Kuo, J. Sun, W.-C. Lee, E. Lim, Y.-R. Guo, and D. M. Barker,
577 2005: Assimilation of Doppler radar observations with a regional 3DVAR system:
578 Impact of Doppler velocities on forecasts of a heavy rainfall case. *J. App. Meteor.*,
579 **44**, 768-788.

580 Xue, M. and J. Dong, 2013: Impact of assimilating best track minimum sea level pressure
581 data together with coastal Doppler radar data on hurricane analysis and prediction
582 at a cloud-resolving resolution. *Acta Meteor. Sinica*, In press.

583 Xue, M., J. Zong, and K. K. Droegemeier, 1996: Parameterization of PBL turbulence in a
584 multi-scale non-hydrostatic model. *Preprint, 11th AMS Conf. Num. Wea. Pred.*,
585 Norfolk, VA, Amer. Metero. Soc., 363-365.

586 Xue, M., K. K. Droegemeier, and V. Wong, 2000: The Advanced Regional Prediction
587 System (ARPS) – A multi-scale nonhydrostatic atmospheric simulation and
588 prediction model. Part I: Model dynamics and verification. *Meteo. Atmos. Phys.*,
589 **75**, 161-193.

590 Xue, M., K. K. Droegemeier, V. Wong, A. Shapiro, and K. Brewster, 1995: *ARPS*
591 *Version 4.0 User's Guide*. [Available at <http://www.caps.ou.edu/ARPS>], 380 pp.

592 Xue, M., K. K. Droegemeier, V. Wong, A. Shapiro, K. Brewster, F. Carr, D. Weber, Y.
593 Liu, and D. Wang, 2001: The Advanced Regional Prediction System (ARPS) – A
594 multi-scale nonhydrostatic atmospheric simulation and prediction tool. Part II:
595 Model physics and applications. *Meteo. Atmos. Phys.*, **76**, 143-165.

596 Zhang, F., Y. Weng, J. A. Sippel, Z. Meng, and C. H. Bishop, 2009: Cloud-Resolving
597 Hurricane Initialization and Prediction through Assimilation of Doppler Radar
598 Observations with an Ensemble Kalman Filter. *Mon. Wea. Rev.*, **137**, 2105-2125.

599 Zhao, K. and M. Xue, 2009: Assimilation of coastal Doppler radar data with the ARPS
600 3DVAR and cloud analysis for the prediction of Hurricane Ike (2008). *Geophys.*
601 *Res. Lett.*, **36**, L12803.

602 Zhao, K., M. Xue, and W. C. Lee, 2012a: Assimilation of GBVTD-retrieved winds from
603 single-Doppler radar for short-term forecasting of super typhoon Saomai (0608) at
604 landfall. *Quart. J. Roy. Meteor. Soc.*, **138**, 1055-1071.

605 Zhao, K., X. F. Li, M. Xue, B. J. D. Jou, and W. C. Lee, 2012b: Short-term forecasting
606 through intermittent assimilation of data from Taiwan and mainland China coastal
607 radars for Typhoon Meranti (2010) at landfall. *J. Geophys. Res.*, **117**, D06108.

608 Zhao, Q. and Y. Jin, 2008: High-Resolution Radar Data Assimilation For Hurricane
609 Isabel (2003) At Landfall. *Bull. Amer. Meteor. Soc.*, **89**, 1355-1372.
610
611

612 Table 1. List of data assimilation and control experiments

613

Experiment	Observations assimilated	Assimilation window (hour)
CNTL	No radar DA	NA
ExpVr2H	V_r	2
ExpTREC2H	V_{TREC}	2
ExpVr1H	V_r	1
ExpTREC1H	V_{TREC}	1
ExpVr3H	V_r	3
ExpTREC3H	V_{TREC}	3
ExpVrZ2H	V_r+Z	2
ExpTRECZ2H	$V_{TREC}+Z$	2

614

615

616 **List of figures**

617 Fig. 1. The physical domain of the numerical simulation, with the average best track
618 (ABT, see section 2) locations plotted every 3 hours from 00 UTC 28 to 0600 UTC
619 29 September 2008 (marked by black dots). The triangle denotes the position of
620 Hualian radar (HLRD), and its observation ranges for radial velocity and radar
621 reflectivity are denoted by dashed and solid circles, respectively. The grey shading
622 indicates terrain height (m).

623 Fig. 2. EnKF data assimilation and forecast flowcharts for all experiments. The vertical
624 arrows denote assimilation of radar data and the slanted arrows at 1800 UTC and
625 2330 UTC denote the addition of two sets of perturbations to generate the ensemble.

626 Fig. 3. The T-TREC analysis at 3 km above the surface at 0000 UTC, 28 September
627 2008. (a) T-TREC retrieved wind vectors overlaid with the observed reflectivity
628 (color shaded, dBz); (b) the observed Doppler radial velocity from HLRD; and (c) the
629 radial velocity calculated from the T-TREC retrieved winds (see section 2). The solid
630 arcs indicate the maximum range of radial velocity data: 230 km from the radar. The
631 '+' denotes the center of the vortex, determined from radar reflectivity.

632 Fig. 4. Top panels: Horizontal wind vectors and speed (color shaded, m s^{-1}) at 3 km
633 height and 0000 UTC, from (a) the GFS analysis, and analyses of (b) ExpVr2H, (c)
634 ExpTREC2H. Middle panels: The sea-level pressure (SLP, contours) and surface
635 wind speed (color shaded, m s^{-1}) at 0200 UTC in (d) CNTL, (e) ExpVr2H, and (f)
636 ExpTREC2H. Minimum SLP is shown at the lower left corner of each figure. Bottom
637 panels: Azimuthally-averaged tangential wind (color shaded) and temperature
638 anomaly (contours with intervals of 2 K) at 0200 UTC for (g) CNTL, (h) ExpVr2H,

639 and (i) ExpTREC2H. The black dot in the panels denotes the observed typhoon
640 center, and the black triangles denote the location of RCHL.

641 Fig. 5. The predicted (a) track, (b) track error, (c) minimum SLP, and (d) maximum
642 surface wind speed from 0200 UTC 28 to 0600 UTC 29 September 2008 for selected
643 experiments, along with the average best track (ABT, see section 2). The dots in (a)
644 denote the center locations every 3-hour starting from 0300 UTC 28. The ABT at
645 0200 UTC 28 is linear interpolated from 0000 and 0300 UTC. The numbers in the
646 legend of panel (b) denote the mean track errors over the 28-hour forecast against the
647 ABT.

648 Fig. 6. Composite reflectivity (color shaded) and wind vectors at 3 km above the surface
649 predicted by (d-f) CNTL, (g-i) ExpVr2H, and (j-l) ExpTREC2H, compared with (a-c)
650 corresponding composite reflectivity observations at (from left to right) 0500, 1100,
651 and 1700 UTC 28 September 2008.

652 Fig. 7. 12-hour accumulated precipitation from 0200 UTC to 1400 UTC for (a)
653 observations, (b) CNTL, (c) ExpVr2H, and (d) ExpTREC2H. The corresponding
654 equitable threat scores for the thresholds of 40 mm (ETS40), 80 mm (ETS80), and
655 120 mm (ETS120) are shown in (b), (c), and (d).

656 Fig. 8. Analysis and forecast minimum sea level pressures MSLP (a), and maximum
657 surface winds (b) during the analysis cycles from 0000 to 0300 UTC. The average
658 best track data and the forecast of CNTL are plotted for comparison.

659 Fig. 9 Analysis increments of tangential wind (colour shaded, m s^{-1}) and pressure
660 (contours with 50 Pa interval) in the east-west vertical cross-section through the

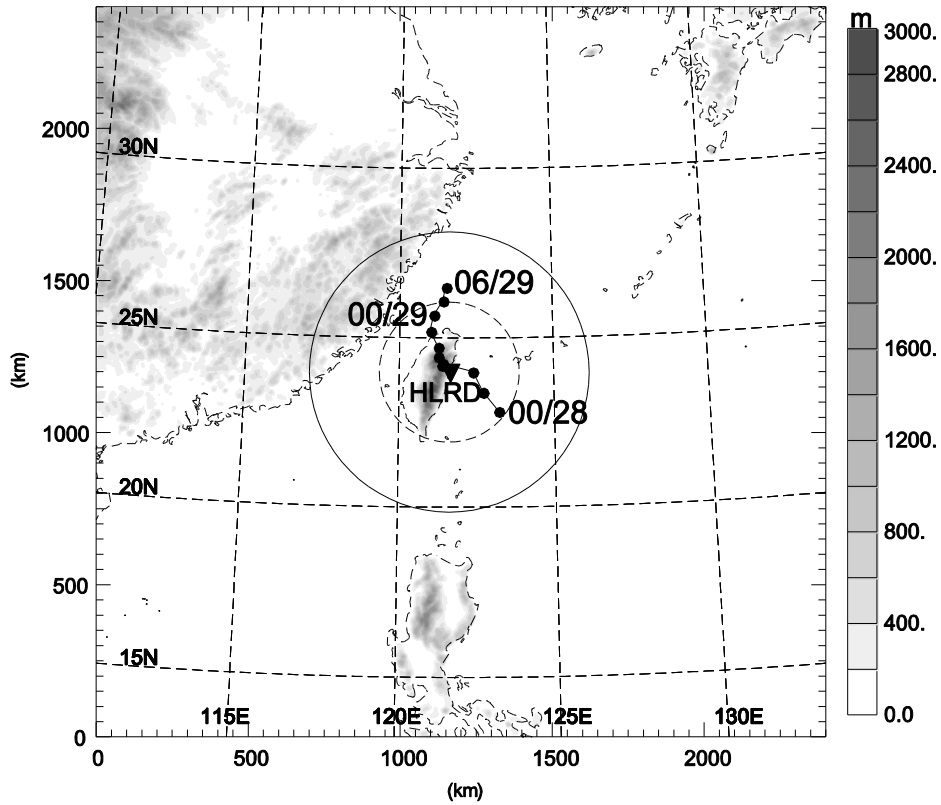
661 analyzed typhoon center from ExpTREC2H, from the first analysis at 0000 UTC 28
662 September 2008.

663 Fig. 10 The root-mean-square of the gradient wind balance residual for the analyses and
664 forecasts from ExpVr3H and ExpTREC3H, during the analysis cycles from 0000 to
665 0300 UTC.

666 Fig. 11. The predicted (a) tracks, (b) track errors, (c) minimum SLPs, and (d) maximum
667 surface wind speeds from 0100 (ExpVr1H, ExpTREC1H), 0200 (ExpVr2H,
668 ExpTREC2H) and 0300 (ExpVr3H, ExpTREC3H) UTC 28 to 0600 UTC 29
669 September 2008, along with the average best track (ABT, see section 2). The dots in
670 (a) denote the center locations every 3-hour starting from 0300 UTC 28. The ABT at
671 0100 and 0200 UTC 28 is linearly interpolated from 0000 and 0300 UTC. The numbers
672 in (b) denote the mean track errors over the 28-hour forecast against the ABT.

673 Fig. 12. The predicted (a) tracks, (b) track errors, (c) minimum SLPs, and (d) maximum
674 surface wind speeds from 0200 UTC 28 to 0600 UTC 29 September 2008 for
675 ExpVr2H, ExpVrZ2H, ExpTREC2H, and ExpTRECZ2H, along with the average best
676 track (ABT, see section 2). The dots in (a) denote the center locations every 3-hour
677 starting from 0300 UTC 28. The ABT at 0200 UTC 28 is linearly interpolated from
678 0000 and 0300 UTC. The numbers in (b) denote the mean track errors over the 28-
679 hour forecast against the ABT.

680

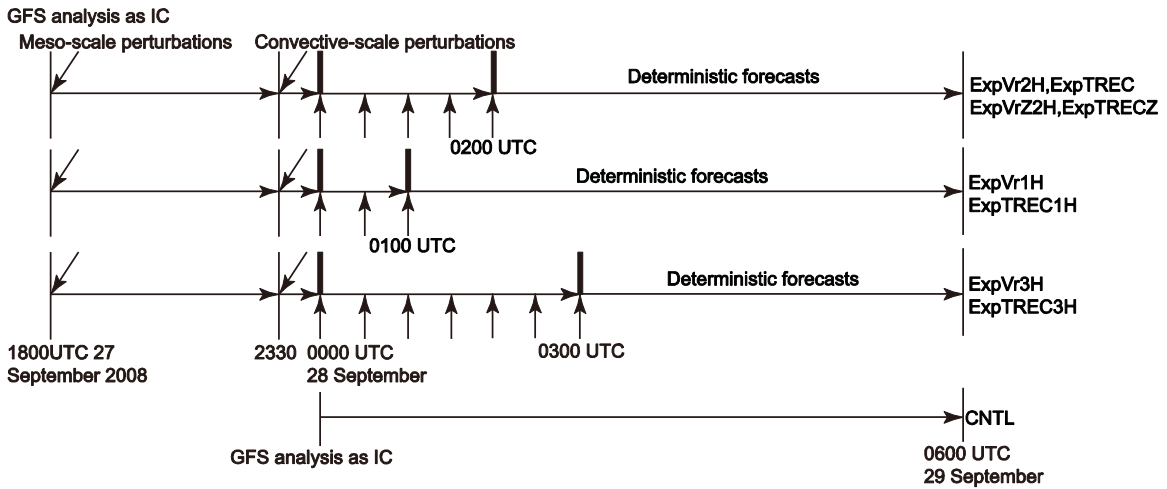


681

682

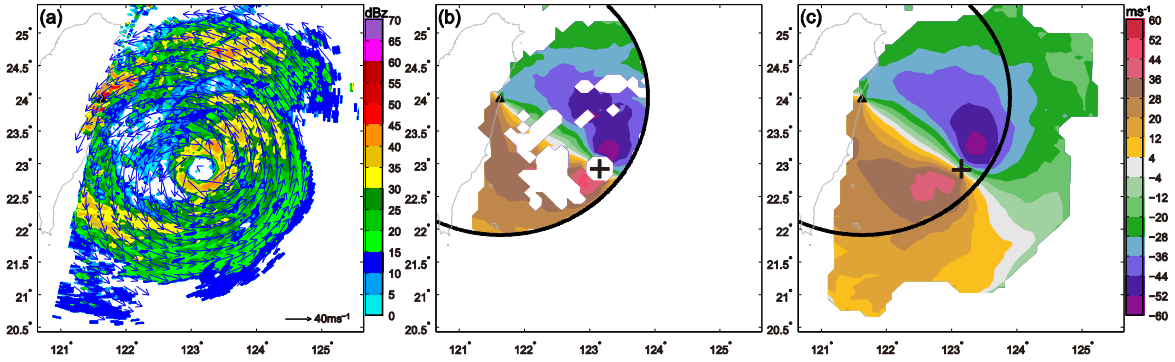
683 Fig. 1. The physical domain of the numerical simulation, with the average best track
 684 (ABT, see section 2) locations plotted every 3 hours from 00 UTC 28 to 0600 UTC 29
 685 September 2008 (marked by black dots). The triangle denotes the position of Hualian
 686 radar (HLRD), and its observation ranges for radial velocity and radar reflectivity are
 687 denoted by dashed and solid circles, respectively. The grey shading indicates terrain
 688 height (m).

689



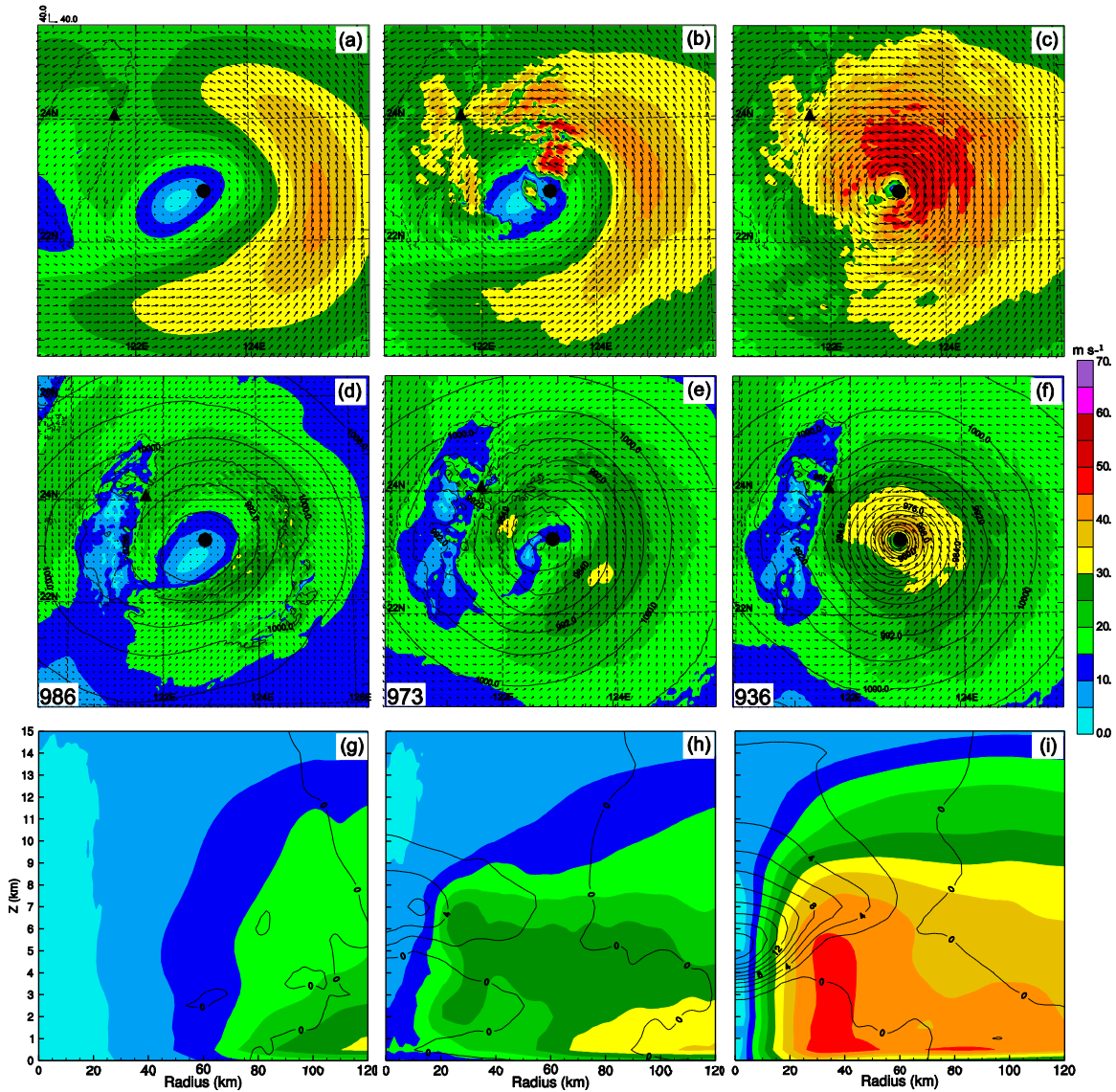
690
 691
 692
 693
 694
 695

Fig. 2. EnKF data assimilation and forecast flowcharts for all experiments. The vertical arrows denote assimilation of radar data and the slanted arrows at 1800 UTC and 2330 UTC denote the addition of two sets of perturbations to generate the ensemble.



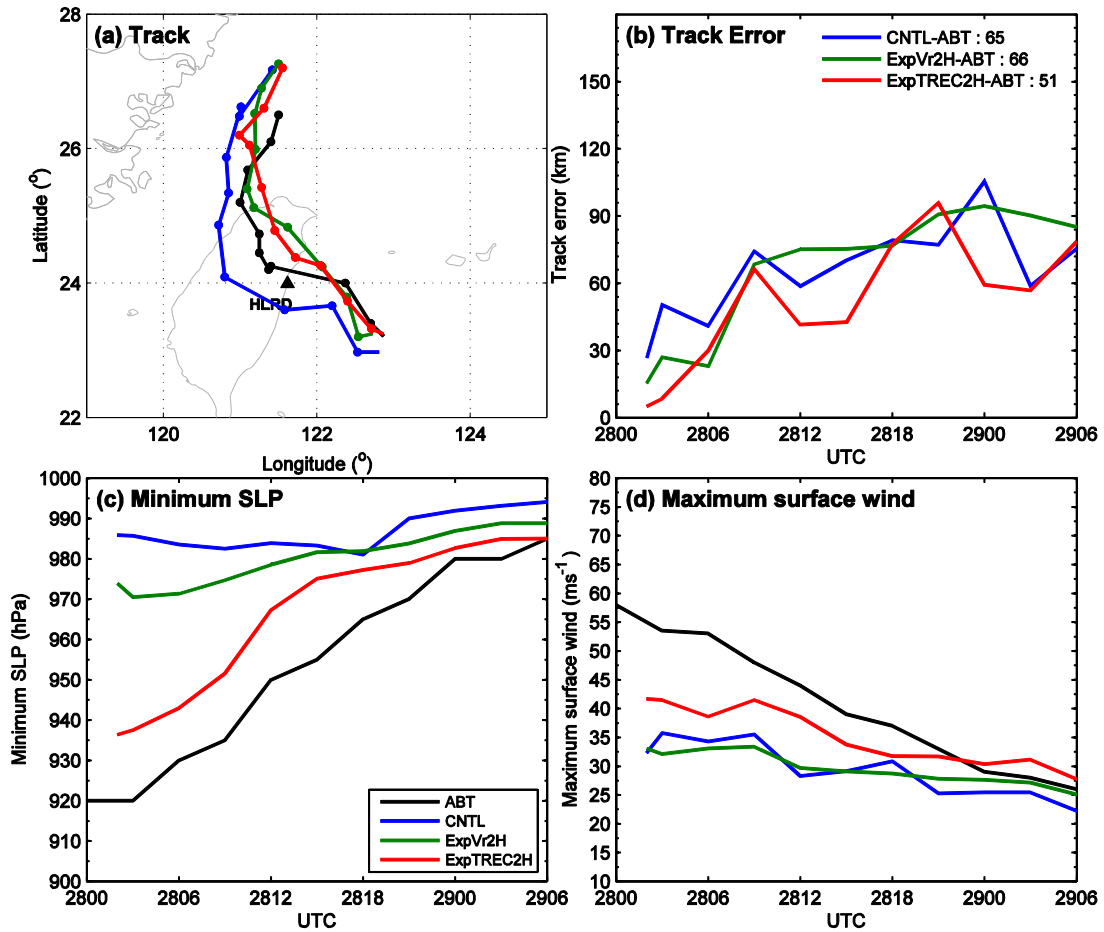
696
 697
 698
 699
 700
 701
 702
 703
 704

Fig. 3. The T-TREC analysis at 3 km above the surface at 0000 UTC, 28 September 2008. (a) T-TREC retrieved wind vectors overlaid with the observed reflectivity (color shaded, dBz); (b) the observed Doppler radial velocity from HLRD; and (c) the radial velocity calculated from the T-TREC retrieved winds (see section 2). The solid arcs indicate the maximum range of radial velocity data: 230 km from the radar. The '+' denotes the center of the vortex, determined from radar reflectivity.



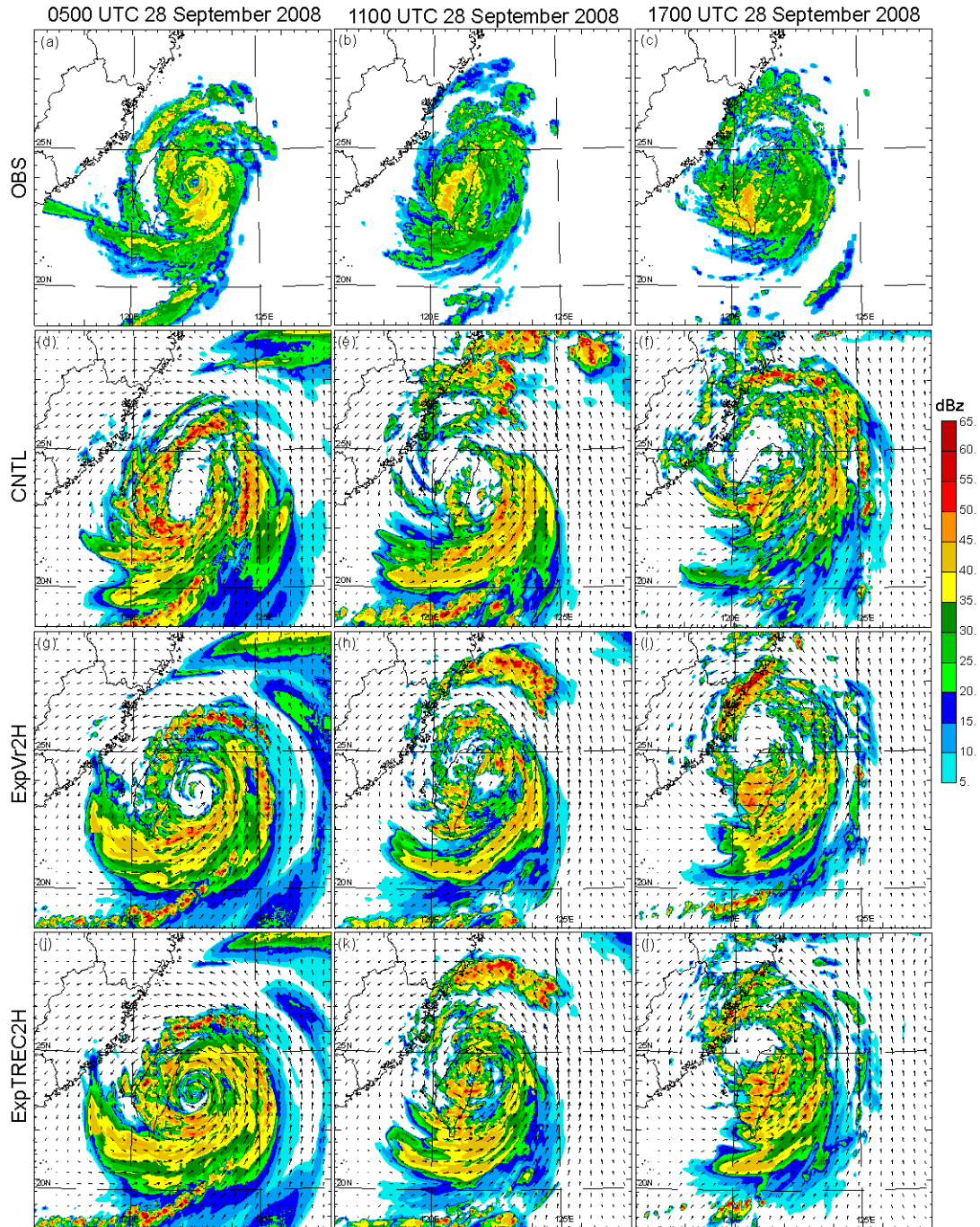
705
 706
 707
 708
 709
 710
 711
 712
 713
 714
 715
 716

Fig. 4. Top panels: Horizontal wind vectors and speed (color shaded, m s^{-1}) at 3 km height and 0000 UTC, from (a) the GFS analysis, and analyses of (b) ExpVr2H, (c) ExpTREC2H. Middle panels: The sea-level pressure (SLP, contours) and surface wind speed (color shaded, m s^{-1}) at 0200 UTC in (d) CNTL, (e) ExpVr2H, and (f) ExpTREC2H. Minimum SLP is shown at the lower left corner of each figure. Bottom panels: Azimuthally-averaged tangential wind (color shaded) and temperature anomaly (contours with intervals of 2 K) at 0200 UTC for (g) CNTL, (h) ExpVr2H, and (i) ExpTREC2H. The black dot in the panels denotes the observed typhoon center, and the black triangles denote the location of RCHL.



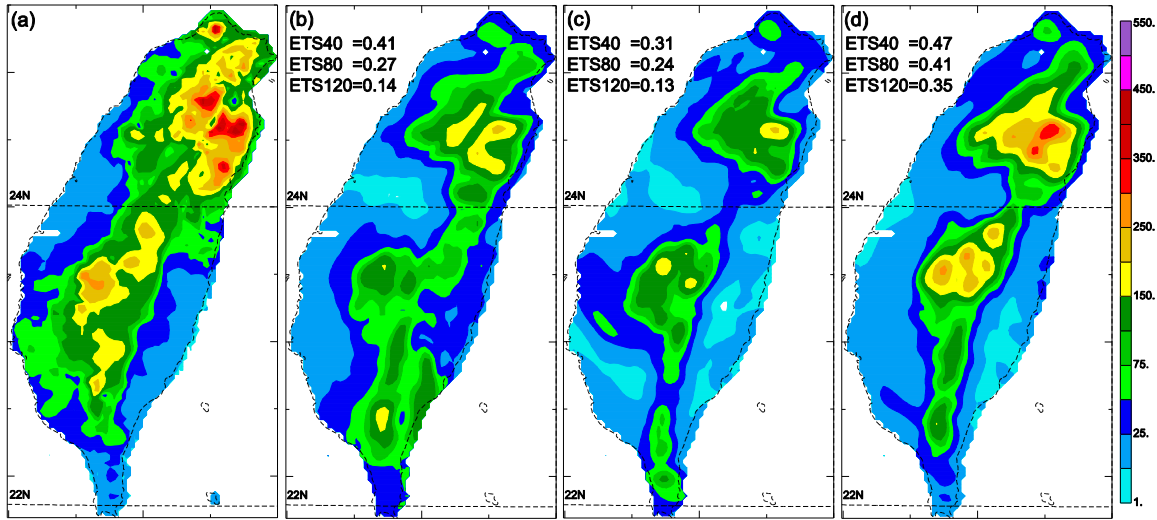
717
 718
 719
 720
 721
 722
 723
 724
 725

Fig. 5. The predicted (a) track, (b) track error, (c) minimum SLP, and (d) maximum surface wind speed from 0200 UTC 28 to 0600 UTC 29 September 2008 for selected experiments, along with the average best track (ABT, see section 2). The dots in (a) denote the center locations every 3-hour starting from 0300 UTC 28. The ABT at 0200 UTC 28 is linear interpolated from 0000 and 0300 UTC. The numbers in the legend of panel (b) denote the mean track errors over the 28-hour forecast against the ABT.



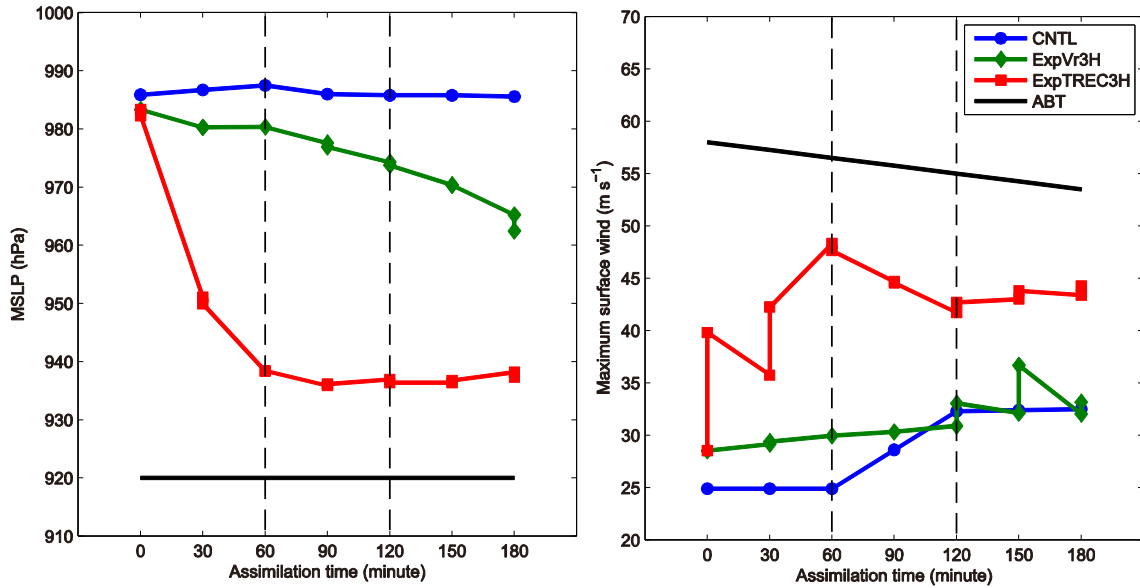
726
 727
 728
 729
 730
 731
 732

Fig. 6. Composite reflectivity (color shaded) and wind vectors at 3 km above the surface predicted by (d-f) CNTL, (g-i) ExpVr2H, and (j-l) ExpTREC2H, compared with (a-c) corresponding composite reflectivity observations at (from left to right) 0500, 1100, and 1700 UTC 28 September 2008.



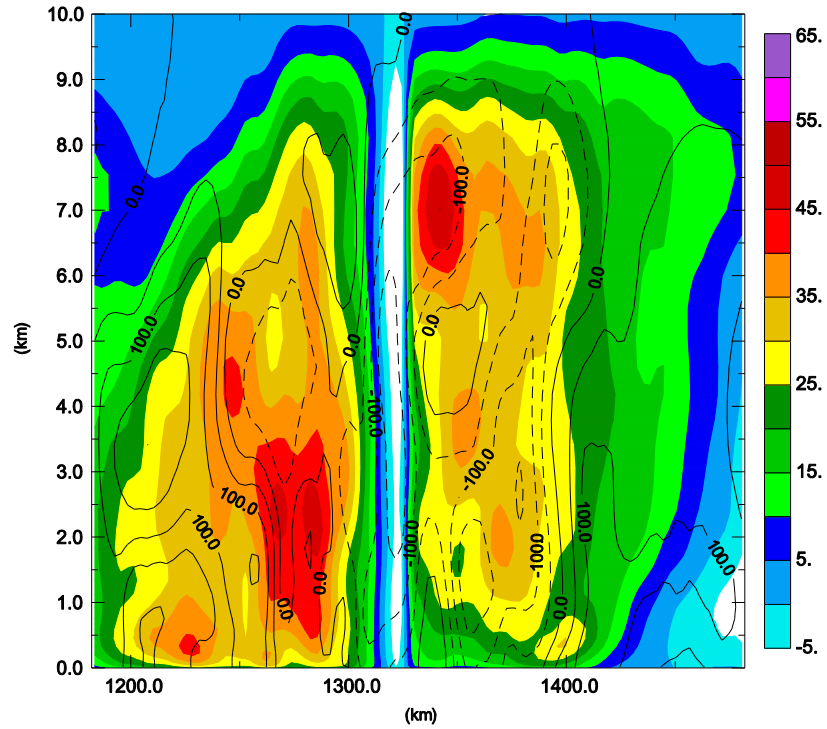
733
 734
 735
 736
 737
 738
 739

Fig. 7. 12-hour accumulated precipitation from 0200 UTC to 1400 UTC for (a) observations, (b) CNTL, (c) ExpVr2H, and (d) ExpTREC2H. The corresponding equitable threat scores for the thresholds of 40 mm (ETS40), 80 mm (ETS80), and 120 mm (ETS120) are shown in (b), (c), and (d).



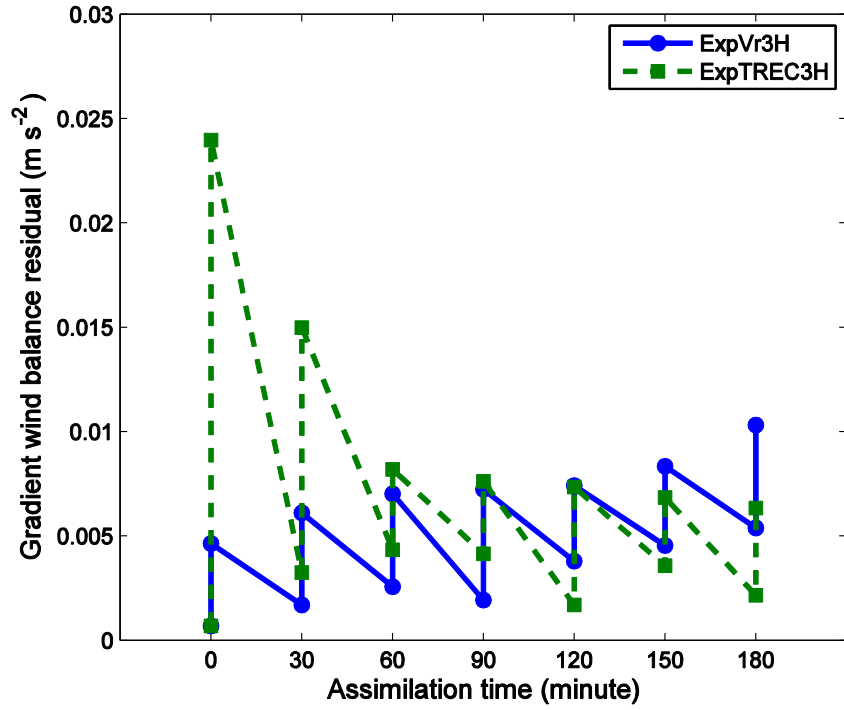
740
 741
 742
 743
 744
 745

Fig. 8. Analysis and forecast minimum sea level pressures MSLP (a), and maximum surface winds (b) during the analysis cycles from 0000 to 0300 UTC. The average best track data and the forecast of CNTL are plotted for comparison.



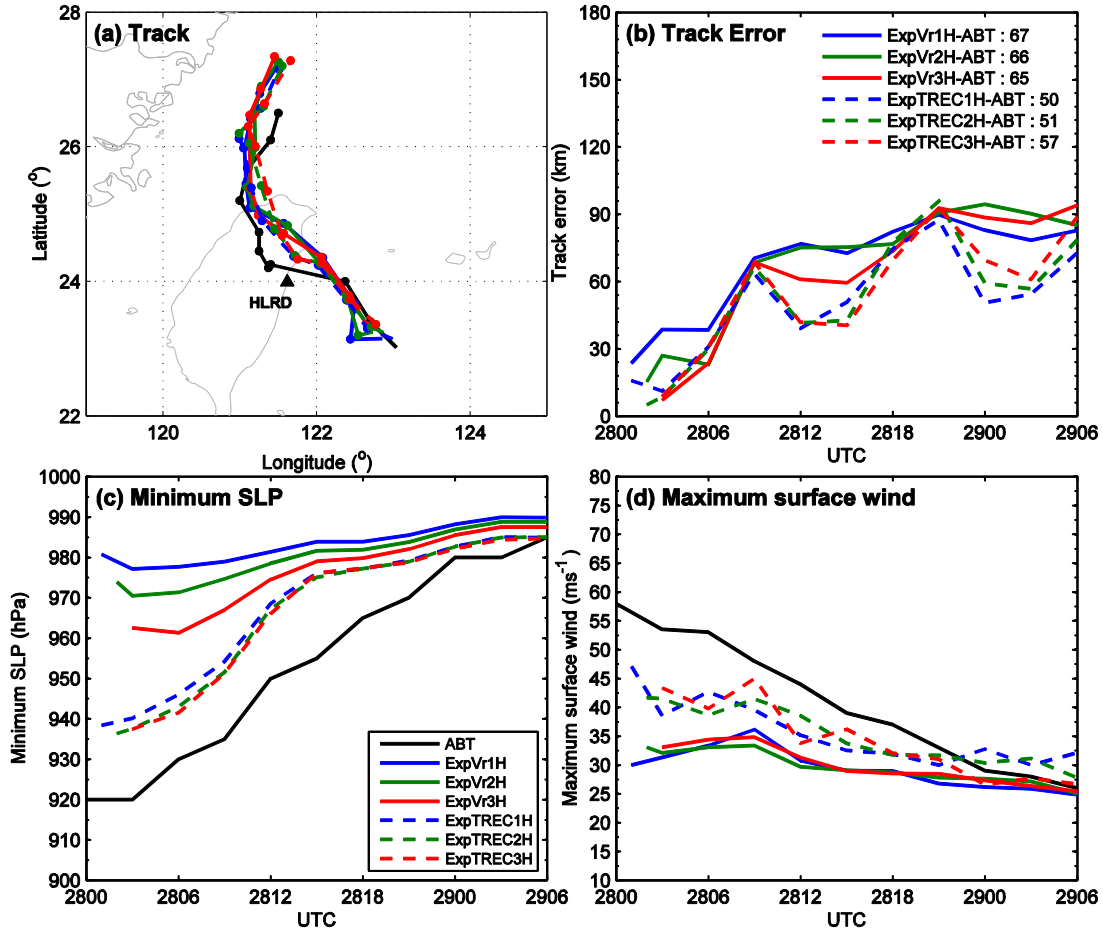
746
 747
 748
 749
 750
 751
 752

Fig. 9 Analysis increments of tangential wind (colour shaded, m s^{-1}) and pressure (contours with 50 Pa interval) in the east-west vertical cross-section through the analyzed typhoon center from ExpTREC2H, from the first analysis at 0000 UTC 28 September 2008.



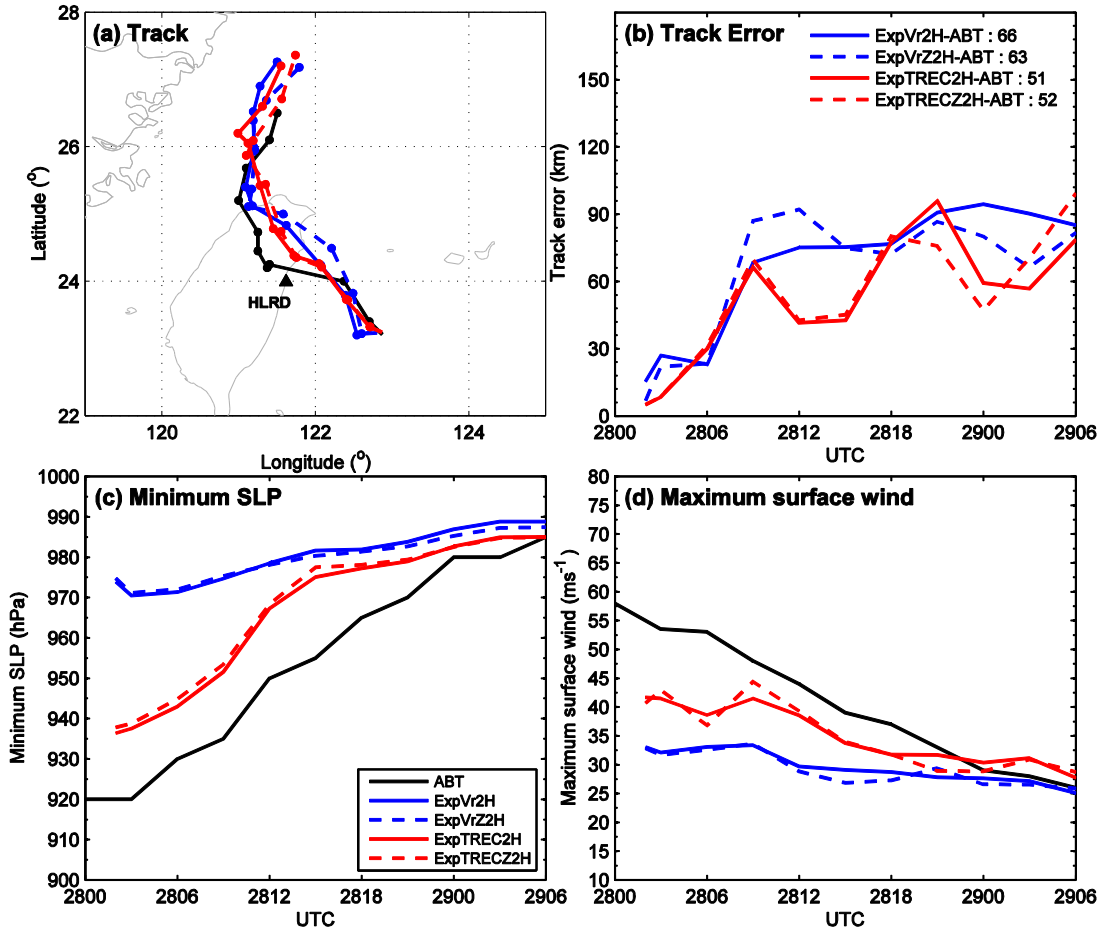
753
 754
 755
 756
 757
 758

Fig. 10 The root-mean-square of the gradient wind balance residual for the analyses and forecasts from ExpVr3H and ExpTREC3H, during the analysis cycles from 0000 to 0300 UTC.



759
760
761
762
763
764
765
766
767
768

Fig. 11. The predicted (a) tracks, (b) track errors, (c) minimum SLPs, and (d) maximum surface wind speeds from 0100 (ExpVr1H, ExpTREC1H), 0200 (ExpVr2H, ExpTREC2H) and 0300 (ExpVr3H, ExpTREC3H) UTC 28 to 0600 UTC 29 September 2008, along with the average best track (ABT, see section 2). The dots in (a) denote the center locations every 3-hour starting from 0300 UTC 28. The ABT at 0100 and 0200 UTC 28 is linear interpolated from 0000 and 0300 UTC. The numbers in (b) denote the mean track errors over the 28-hour forecast against the ABT.



769
 770
 771
 772
 773
 774
 775
 776
 777
 778
 779

Fig. 12. The predicted (a) tracks, (b) track errors, (c) minimum SLPs, and (d) maximum surface wind speeds from 0200 UTC 28 to 0600 UTC 29 September 2008 for ExpVr2H, ExpVrZ2H, ExpTREC2H, and ExpTRECZ2H, along with the average best track (ABT, see section 2). The dots in (a) denote the center locations every 3-hour starting from 0300 UTC 28. The ABT at 0200 UTC 28 is linearly interpolated from 0000 and 0300 UTC. The numbers in (b) denote the mean track errors over the 28-hour forecast against the ABT.